

Binary Huygens' Metasurfaces: Experimental Demonstration of Simple and Efficient Near-Grazing Retroreflectors for TE and TM Polarizations

Alex M. H. Wong, *Member, IEEE*, Philip Christian[✉], and George V. Eleftheriades, *Fellow, IEEE*

Abstract—This paper investigates the retroreflective properties of a type of periodic metasurface, which is aggressively discretized to include only two cells per grating period. The resultant metasurface, which we term the binary Huygens' metasurface, dramatically simplifies the design toward highly efficient, low cost, and robust metasurface retroreflectors. Using this discretization method, we designed, simulated, and measured two binary Huygens' metasurfaces that retroreflect an incident plane wave at 82.87° from broadside, for TE and TM polarized waves, respectively. The simulated results for a 2-D infinite structure show power efficiencies of 94% (TE) and 99% (TM). The measured results show a power efficiency of 93% for both TE and TM polarizations. This shows that it is possible to obtain a high retroreflection power efficiency at an angle of choice using a very simple (slot or patch) metasurface design. The proposed design methodology allows one to achieve not only retroreflection but also reflection to arbitrary angles, with very high efficiency, which diversifies its uses.

Index Terms—Binary surfaces, equivalence principle, Huygens' sources, metasurface, retroreflector.

I. INTRODUCTION

A RETROREFLECTOR is a device that back reflects an electromagnetic wave in the direction of incidence. The passive retroreflection of electromagnetic waves, from radio to optical frequencies, finds a myriad of practical applications in communication with satellites and unmanned aerial vehicles [1]–[3], remote sensing [4], target labeling, navigation safety, and radar cross section (RCS)/visibility enhancement [5], [6]. In these and other applications, it is often desirable to have retroreflectors which: 1) operate at large angles of oblique incidence; 2) can handle TE and TM polarizations; 3) low profile; 4) lightweight; 5) low loss; and 6) can be practically manufactured. In the following, we survey prominent classes of retroreflectors in view of the aforementioned factors.

The simplest retroreflection structure is a metallic plate. Clearly, a metallic plate, with side lengths of several wavelengths and beyond, is a strong retroreflector when the incident

wave impinges from a direction normal to the plate, but a poor retroreflector otherwise. Other elementary metallic structures—such as the cylinder or the sphere—have been amply studied. As expected, they feature weaker retroreflection strengths, but the retroreflection levels remain the same as the incident wave's direction varies in the azimuthal plane for the cylinder and across all angles for the sphere [7]. Perhaps, the most efficient metallic retroreflection structure is the corner cube, as illustrated in Fig. 1(a). By connecting two (or three) metallic plates at right angles, one forms a reflection structure where the incoming wave is reflected two (or three) times and achieves retroreflection. Theoretical and experimental works show that the corner cube provides efficient retroreflection in the range of $\pm 15^\circ$ [8], [9]. The main disadvantages of the corner cube are: 1) the structure is large: its depth is appreciable compared to the size of the aperture; 2) it cannot support retroreflection beyond a maximum angle of 45° ; and 3) in some cases, it is reported to alter the polarization of an incoming wave [8], [10]. Using a sheet built from an array of 2-D array of small trihedral corner cubes, one can significantly reduce the depth of the retroreflection structure, and achieves appreciable retroreflection in the range of $\pm 30^\circ$ [11]. Nevertheless, efficient retroreflection remains out of reach at large oblique angles.

Another class of retroreflectors involves dielectric and/or plasmonic materials. It has been found that for a random array of spherical (or near-spherical) scatterers, a coherent backscattering phenomenon occurs to strengthen retroreflection [12], [13]. Under favorable conditions, a retroreflection strength as high as 40% has been observed [12]. A similar effect occurs for random rough surfaces [14]. Essentially, these configurations encourage multiple scattering, and thereby strengthen the retroreflected wave component that achieves phase alignment across multiple paths [13]. The cat's eye retroreflector [see Fig. 1(b)]—a convex dielectric lens placed one focal length away from a (ideally parabolic) mirror—has received considerable attention [10], [15]–[17]. Similar to the corner cube, the cat's eye retroreflector has a depth that is comparable to its lateral size. However, since the wave is focused to a considerably smaller area at the location of the mirror, this configuration is useful for performing switching and encoding on an electromagnetic signal. Biermann *et al.* [10] have demonstrated a cat's eye retroreflector with a multistage lens, which achieved highly efficient retroreflection across the range of $\pm 15^\circ$. Lundvall and Nikolajeff [17] demonstrated a cat's eye

Manuscript received October 29, 2017; revised February 22, 2018; accepted March 4, 2018. Date of publication March 16, 2018; date of current version May 31, 2018. This work was supported by an NSERC Collaborative R&D Grant with Thales Canada. (Corresponding author: George V. Eleftheriades.)

The authors are with the Edward S. Rogers Sr. Department of Electrical and Computer Engineering, University of Toronto, Toronto, ON M5S 3G4, Canada (e-mail: gelefh@waves.utoronto.ca).

Color versions of one or more of the figures in this paper are available online at <http://ieeexplore.ieee.org>.

Digital Object Identifier 10.1109/TAP.2018.2816792

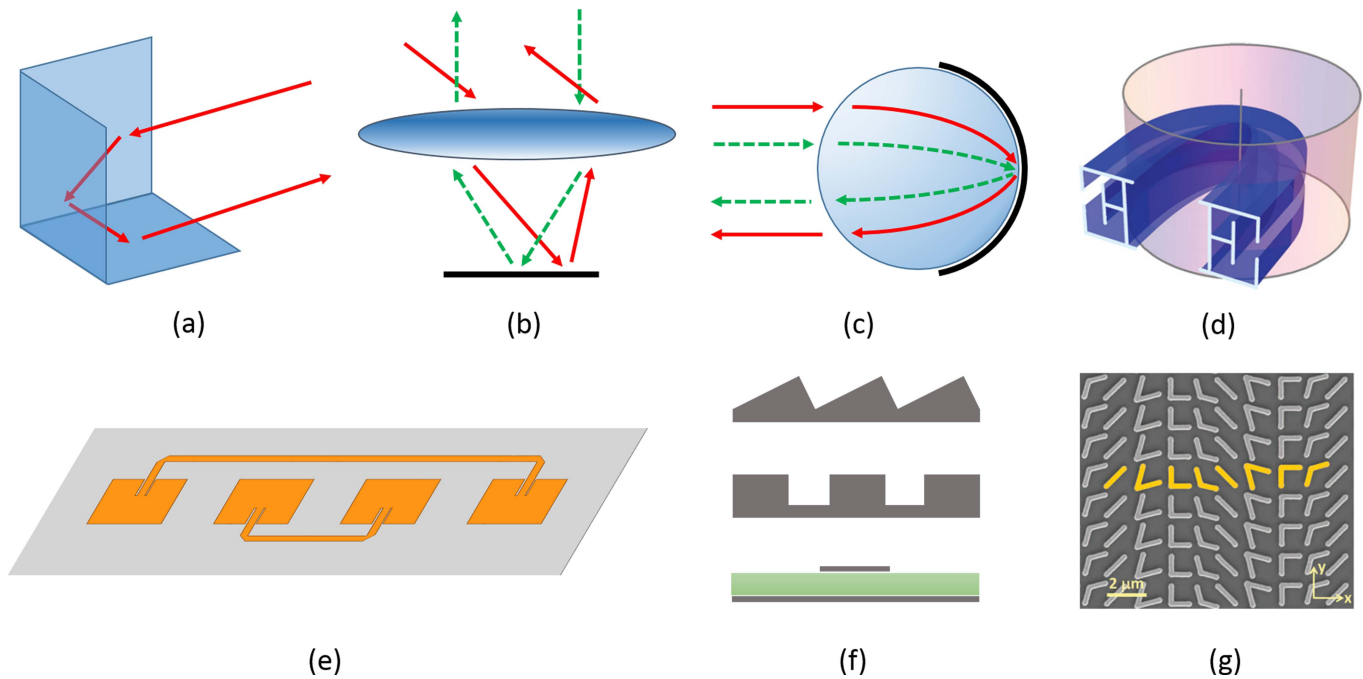


Fig. 1. Retroreflection devices. (a) Metallic corner cube. (b) Cat's eye retroreflector. Black line: metallic mirror. (c) Luneburg lens backed by a metallic mirror. In (a)–(c), arrows outline representative trajectories of electromagnetic rays. (d) Eaton's lens. Reprinted by permission from Macmillan Publishers Ltd.: Nature Materials [19], copyright 2009. (e) Four-element Van Atta patch antenna array. (f) Various metallic gratings that include the echellette grating (top), the groove grating (middle), and the strip grating (bottom). Gray: metal. Green: dielectric substrate. (g) Representative metasurface from [23]. Reprinted with permission from American Association for the Advancement of Science.

retroreflector with an array of microlenses and micromirrors. This device was relatively low profile, and achieved efficient retroreflection across an angular range of $\pm 30^\circ$. By replacing the convex lens and the lens–mirror spacing with a Luneburg lens [18], one arrives at the Luneburg lens retroreflector [see Fig. 1(c)], which when properly designed can facilitate efficient retroreflection across a wide angular range of about $\pm 50^\circ$ [9]. While the Luneburg lens retroreflector has seen some practical applications, it is limited by its large size, heavy weight, and relatively expensive fabrication. More exotic metallodielectric retroreflectors have been proposed, which include an Eaton lens [19] [see Fig. 1(d)] and a retroreflection superscatterer [20] implemented through the transformation optics approach, and a plasmonic superscatterer which is essentially a superdirective small antenna, impedance matched by metal and dielectric shells of precise thickness [21], [22]. While interesting and potentially efficient, these proposals require very high precision in the dimension and permittivity of the materials involved. Their practicality is yet to be proved beyond proof-of-principle laboratory demonstrations.

The Van Atta array is a practical and low-profile wide angle retroreflector for RF electromagnetic waves [24], [25]. Fig. 1(e) shows a four-element Van Atta array with proper connections amongst the antenna patches. The antennas on the surface are designed to efficiently couple to the incident and reflected waves; the crossed transmission line connections reverse the phase front on the surface of the retroreflector. Thus together, the antennas and their connections serve to reverse the phase front along the surface of the retroreflector, and thereby achieve retroreflection. The Van Atta array has

been shown to work in 1-D and 2-D configurations [25] and on both planar and curved surfaces [26]. A wide angular bandwidth of over $\pm 60^\circ$ has also been demonstrated [9]. However, the Van Atta array suffers a few drawbacks. First, unlike many previous devices, the Van Atta array relies on the near-resonant operation of antenna elements. Hence, its operation bandwidth is limited by the antenna elements, and its angular range is limited by the element factor. Similarly, due to limitations from the antenna elements and the transmission lines, it is difficult to imagine its extension to frequencies beyond the millimeter-wave regime. Additionally, the criss-crossed connections between antenna elements greatly complicate antenna routing as the array size increases. This makes the Van Atta array impractical for a retroreflector with an aperture length of several wavelengths and beyond.

When the incident wave direction is known, a metallic grating can be designed as a practical, low profile, and efficient retroreflector. Gratings used for retroreflection purposes are known as blazed gratings; three prominent kinds of blazed gratings are depicted in Fig. 1(f) and explained as follows. Traditional echelette gratings have been designed to support blazed reflection [27], however, it has been found that their saw-tooth edges lead to spurious undesired diffraction and limitations, particularly for retroreflecting TM waves. Gratings featuring metallic grooves, on the other hand, are found to support efficient retroreflection for both TE and TM waves [28], [29]. It has since been found that a metallic strip grating atop a metal-backed substrate [30], [31] functions similar to the metallic groove grating [30], and hence, can serve as efficient retroreflectors for both TE and TM

polarizations [32]–[34]. However, a few reports have emerged on the usage of these retroreflectors at large angle incidence of beyond $\pm 60^\circ$, thus their effectiveness for near-grazing incidence is yet to be investigated.

More recently, the metasurface [Fig. 1(g)] has emerged as a versatile tool in electromagnetic wavefront manipulation [23], [35]–[39]. By tuning the surface impedance as a function of position, various wavefront operations have been demonstrated [40], which modify the amplitude [41], phase [41], [42], polarization [43], [44], and propagation direction [42], [45] of an incident wave. Specifically, metasurfaces with linear phase variants have been demonstrated: they represent low profile and cost-effective structures, which can perform retroreflections at selected angles. Additionally, they provide more freedom in waveform manipulation than a grating which is inherently 1-D. Nevertheless, to date most demonstrated metasurfaces feature finely discretized surface impedance profiles implemented by element cells of size $\lambda/8$ or smaller. This means that the scaling of these metasurfaces for use at higher frequencies will involve high-precision fabrication, which may drive up the fabrication cost, reduce the metasurface's robustness, or render impossible altogether the scaling of the technology. Moreover, the near-grazing angle operation of a metasurface has seldom been reported, and its power efficiency is yet to be investigated.

In this paper, we report the design and demonstration of near-grazing angle retroreflection metasurfaces for both TE and TM polarizations. Our proposed structure is a subwavelength array of rods (for TE) and slot (for TM) backed by a ground plane, etched onto a dielectric substrate. The proposed metasurface synthesizes a grating with an ultra-coarse discretization of two cells per grating period. Such aggressive discretization alleviates, as much as possible, the need for small features, and paves the way to a simple metasurface retroreflector that is highly efficient, robust, cost-efficient, and easily scalable to millimeter-wave and tetrahertz frequencies. The rest of this paper is organized as follows. In Section II, we formulate our problem and present our metasurface design methodology. In Section III, we show designs and full-wave simulation results for the TE and TM retroreflection metasurfaces. For the TM case, we also examine the origin of spurious effects that are not observed for the TE counterpart. In Section IV, we report monostatic and bistatic RCS experimental results which validate simulations and demonstrate the operation of both metasurfaces. Finally, in Section V, we conclude our findings.

II. METASURFACE DESIGN METHODOLOGY

In this paper, we adopt a surface impedance approach to metasurface design, demonstrated in [39], [45], and [46]. In this section, we first determine the necessary impedance (and reflection coefficient) profile for the retroreflection metasurface, then examine the effects of discretization on the performance of the metasurface.

A. Surface Impedance Analysis

Fig. 2 illustrates plane wave diffraction with a generalized metasurface for both the TM and TE incident polarizations.

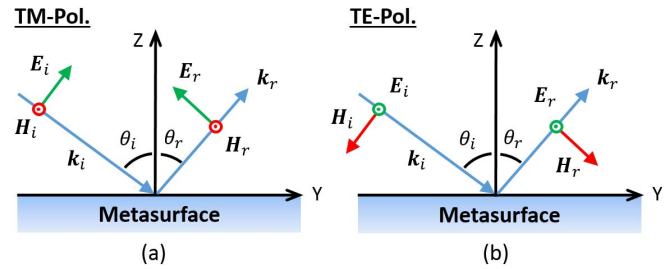


Fig. 2. Diagrams of (a) TM and (b) TE single-plane wave reflection off a metasurface at $z = 0$.

We will find the necessary impedance profile for this surface, and thereafter specialize to the case of retroreflection, where $\theta_r = -\theta_i$.

We shall analyze the TM case [Fig. 2(a)] in detail. In the illustration of [Fig. 2(a)], the incident and reflected plane waves can be described, respectively, as

$$\begin{aligned} \mathbf{E}_i &= E_{i0} \exp(-jk_0(\sin \theta_i y - \cos \theta_i z)) \\ &\quad \cdot (\cos \theta_i \hat{\mathbf{y}} + \sin \theta_i \hat{\mathbf{z}}), \\ \mathbf{H}_i &= \frac{E_{i0}}{\eta} \exp(-jk_0(\sin \theta_i y - \cos \theta_i z)) \hat{\mathbf{x}} \end{aligned} \quad (1)$$

and

$$\begin{aligned} \mathbf{E}_r &= E_{r0} \exp(-j(k_0(\sin \theta_r y + \cos \theta_r z) + \phi)) \\ &\quad \cdot (-\cos \theta_r \hat{\mathbf{y}} + \sin \theta_r \hat{\mathbf{z}}), \\ \mathbf{H}_r &= \frac{E_{r0}}{\eta} \exp(-j(k_0(\sin \theta_r y + \cos \theta_r z) + \phi)) \hat{\mathbf{x}} \end{aligned} \quad (2)$$

where $k_0 = 2\pi/\lambda_0$ is the spatial frequency and λ_0 is the free space wavelength. ϕ is a constant phase offset between the incident and reflected waves at $y = 0$, which remains arbitrary for the moment. The fields tangential to the surface (at $z = 0^+$) are hence described as follows:

$$\begin{aligned} \mathbf{E}_{i,\text{tan}} &= E_{i0} \cos \theta_i \exp(-jk_0 \sin \theta_i y) \hat{\mathbf{y}} \\ \mathbf{H}_{i,\text{tan}} &= \frac{E_{i0}}{\eta} \exp(-jk_0 \sin \theta_i y) \hat{\mathbf{x}} \\ \mathbf{E}_{r,\text{tan}} &= -E_{r0} \cos \theta_r \exp(-j(k_0 \sin \theta_r y + \phi)) \hat{\mathbf{y}} \\ \mathbf{H}_{r,\text{tan}} &= \frac{E_{r0}}{\eta} \exp(-j(k_0 \sin \theta_r y + \phi)) \hat{\mathbf{x}}. \end{aligned} \quad (3)$$

We will introduce two relationships at this point that will simplify the derivation that follows. First, we will define

$$\Delta \Phi(y) = k_0(\sin \theta_r - \sin \theta_i)y + \phi \quad (4)$$

as the phase difference between the incident and reflected plane waves. Next, we set

$$E_{r0} = \sqrt{\frac{\cos \theta_i}{\cos \theta_r}} E_{i0} \quad (5)$$

which relates the incident and reflected plane wave amplitudes for perfect reflection metasurfaces [39], [40]. Using (4) and (5), we write the surface impedance (as a function of location on the metasurface) which will generate the desired

reflection upon the prescribed incidence

$$\begin{aligned} Z_{s,\text{TM}} &= \frac{\mathbf{E}_{\text{tan}} \cdot \hat{\mathbf{y}}}{\mathbf{H}_{\text{tan}} \cdot \hat{\mathbf{x}}} = \frac{(\mathbf{E}_{i,\text{tan}} + \mathbf{E}_{r,\text{tan}}) \cdot \hat{\mathbf{y}}}{(\mathbf{H}_{i,\text{tan}} + \mathbf{H}_{r,\text{tan}}) \cdot \hat{\mathbf{x}}} \\ &= \eta \frac{\cos \theta_i \sqrt{\cos \theta_r} - \cos \theta_r \sqrt{\cos \theta_i} e^{-j \Delta \Phi(y)}}{\sqrt{\cos \theta_r} + \sqrt{\cos \theta_i} e^{-j \Delta \Phi(y)}}. \end{aligned} \quad (6)$$

For the case of retroreflection, $\theta_r = -\theta_i \Rightarrow \cos \theta_r = \cos \theta_i$. Redefining $\theta = |\theta_i| = |\theta_r|$, we obtain

$$\begin{aligned} Z_{s,\text{TM}} &= \eta \cos \theta \left(\frac{1 - e^{-j \Delta \Phi(y)}}{1 + e^{-j \Delta \Phi(y)}} \right) \\ &= j Z_{0,\text{TM}} \tan \left(\frac{\Delta \Phi(y)}{2} \right) \end{aligned} \quad (7)$$

where $Z_{0,\text{TM}} = \eta \cos \theta$ is the wave impedance for the incident and reflected waves in TM polarization.

It is often convenient to work with reflection coefficients as opposed to surface impedances. In this single plane wave retroreflection scenario, one straightforwardly finds the reflection coefficient as

$$\Gamma_{\text{TM}} = \frac{Z_{s,\text{TM}} - Z_{0,\text{TM}}}{Z_{s,\text{TM}} + Z_{0,\text{TM}}} = -e^{-j \Delta \Phi(y)}. \quad (8)$$

One can find corresponding relationships for the TE polarization following a procedure very similar to the one described earlier. We refer the interested reader to [39] where reflection with this polarization is discussed in more detail. Following the analysis outlined earlier, we find that for the TE polarized single-wave reflection scenario [Fig. 2(b)], the surface impedance as

$$Z_{s,\text{TE}} = \frac{\eta}{\sqrt{\cos \theta_i \cos \theta_r}} \frac{\sqrt{\cos \theta_r} + \sqrt{\cos \theta_i} e^{-j \Delta \Phi(y)}}{\sqrt{\cos \theta_i} - \sqrt{\cos \theta_r} e^{-j \Delta \Phi(y)}}. \quad (9)$$

Specifically, for retroreflection, (9) reduces to

$$Z_{s,\text{TE}} = -j Z_{0,\text{TE}} \cot \left(\frac{\Delta \Phi(y)}{2} \right) \quad (10)$$

where $Z_{0,\text{TE}} = \eta / \cos \theta$ is the wave impedance for TE polarized incident and reflected waves. The corresponding reflection coefficient is

$$\Gamma_{\text{TE}} = \frac{Z_{s,\text{TE}} - Z_{0,\text{TE}}}{Z_{s,\text{TE}} + Z_{0,\text{TE}}} = e^{-j \Delta \Phi(y)} = -\Gamma_{\text{TM}}. \quad (11)$$

Relationships akin to (6) and (9) have been derived, to various degrees of generality, in [39] and [45]. Additionally, one may simplistically (and correctly) assume from grating theory that the desired reflection coefficient profile is that of a linear phase gradient, as shown in (8) and (11). Nevertheless, the preceding analysis shows, with the full rigor of Maxwell's equations, that it is possible to retroreflect all the power from an incident plane wave, at any incidence angle and with either polarization. Moreover, such perfect retroreflection is achieved using an aptly designed *passive* metasurface with surface impedances described by (6) and (9), or equivalently with reflection coefficients described by (8) and (11).

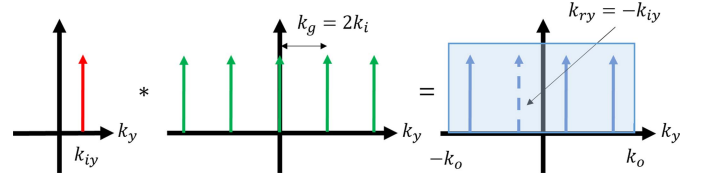


Fig. 3. Transformation of a plane wave's transverse (y-directed) wave vector, as it is reflected from a periodic metasurface. Arrows: spatial frequencies of possible spectral components, but their lengths do not reflect the relative amplitudes of these components.

B. Discretization Effects

Next, we examine the degree of discretization suitable for our realization of the retroreflection metasurface. Whilst most metasurfaces are designed in a continuous manner, their implementations are often facilitated by discretizing into subwavelength-sized cells, each of which are implemented to achieve the requisite electromagnetic property (e.g., surface susceptibility or surface impedance). Individual cases, such as [47], have shown that coarser discretization is possible for selected reflection surfaces. A coarse discretization benefits metasurface design in two major ways: they reduce the mutual coupling between metasurface elements and relax tolerance requirements, allowing for cost-effective and robust metasurface fabrication well into the millimeter wave frequencies. In the following, we shall provide a brief investigation toward the proper design of an aggressively discretized retroreflection metasurface.

Fig. 3 shows the transformation of a plane wave's transverse (y-directed) spatial frequency as it reflects off a retroreflection metasurface. The reflected wave's spatial frequencies map straightforwardly into the angular domain through

$$\sin \theta = \frac{k_y}{k_0} \quad \text{for } k_y \leq k_0. \quad (12)$$

Fig. 3 (arrows) shows the presence of spectral components, but do not represent the amplitudes or phases of these spectral components. As seen, the periodic metasurface produces a series of diffraction orders which can, in general, reflect off different directions. The transverse spatial frequencies of diffracted orders are given as

$$k_{my} = k_{iy} + m k_g = k_{iy} + m \frac{2\pi}{\Lambda_g} \quad (13)$$

where k_{iy} represents the y-directed spatial frequency of the incident wave, while k_g and Λ_g , respectively, represent the spatial frequency and the period of the metasurface.

To generate a retroreflection metasurface, one tunes the $m = -1$ diffraction order into the retroreflection order by choosing Λ_g appropriately

$$k_{ry} = k_{iy} - \frac{2\pi}{\Lambda_g} = -k_{iy} \Rightarrow \Lambda_g = \frac{\lambda_0}{2 \sin \theta_i}. \quad (14)$$

For a successful metasurface—a metasurface that implements the surface impedance profile (6) and/or (9)—power diffraction will maximize for the retroreflection mode and vanish for other propagating modes.

With Λ_g , and thereby k_g , fixed to achieve retroreflection at a predefined angle, there exists a fixed number of reflected propagation waves, as shown pictorially in Fig. 3 by the spectral components k_{ry} which reside within the propagation region $[-k_0, k_0]$. The number of such diffraction orders is given as

$$N = 1 + \left\lfloor \frac{k_0 - k_i}{k_g} \right\rfloor + \left\lfloor \frac{k_0 + k_i}{k_g} \right\rfloor \quad (15)$$

where $\lfloor \cdot \rfloor$ is the floor (round down) operator. It can be reasoned that the maximal metasurface discretization requires at least N cells per metasurface period, to provide sufficient degrees of freedom to tune the amplitude and phase of each diffraction order. (This can be mathematically proven through a Fourier analysis, which we defer to a forthcoming work.) For a retroreflector, the discretization requirement can be further relaxed to

$$N = 2 \times \left\lceil \frac{k_0}{k_g} \right\rceil \quad (16)$$

where $\lceil \cdot \rceil$ is the rounding operator. Combining (12), (14), and (16), we see that for a sufficiently large angle incidence

$$\theta_i \geq 19.5^\circ \Rightarrow k_g > \frac{2}{3}k_0 \Rightarrow N = 2. \quad (17)$$

Hence, for angles of incidence beyond 19.5° , the retroreflection metasurface can be most aggressively discretized to have only *two cells* per grating period. (This case for minimum discretization concurs with an earlier work [28] on blazed gratings.) We name the resultant surface a binary Huygens' metasurface—a metasurface with effective electric and magnetic behavior comprising only two metasurface cells. As a practical design choice, we space these metasurface cells in equidistant fashion across the metasurface period (i.e., adjacent cells are spaced half a period apart). Based on this spacing, an application of (8) and (11) shows that these two cells should exhibit uniform reflection amplitude and 180° relative phase shift—irrespective of the desired angle of retroreflection. In Section III, we will describe the design and simulation of TE and TM metasurfaces which achieve these properties.

III. DESIGN AND SIMULATION

Fig. 4 depicts the geometry of our desired metasurface. A typical smooth surface reflects in the specular direction, whereas our desired metasurface reflects strongly in the retro direction. For the TE polarization, the E -field of all plane waves points to the x -direction; for the TM polarization, the H -field of all plane waves points to the x -direction. We aim to design a metasurface that emanate two diffraction orders—the specular ($m = 0$) and retroreflection ($m = -1$) orders; by appropriate metasurface design, we aim to significantly suppress specular reflection and, hence, create an efficient retroreflector. In this paper, a 24 GHz incident wave impinges on the metasurface at a near-grazing incidence angle of $\theta_i = 82.87^\circ$ with respect to normal. Using (14), we obtain

$$\Lambda_g = 6.30 \text{ mm}. \quad (18)$$

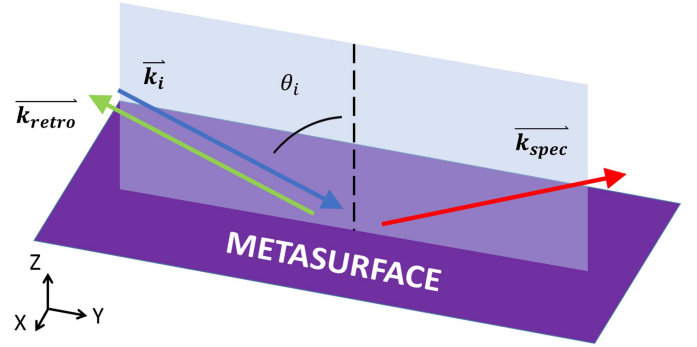


Fig. 4. Illumination scenario of the desired metasurface, which should minimize specular reflection (red arrow) and maximize retroreflection (green arrow).

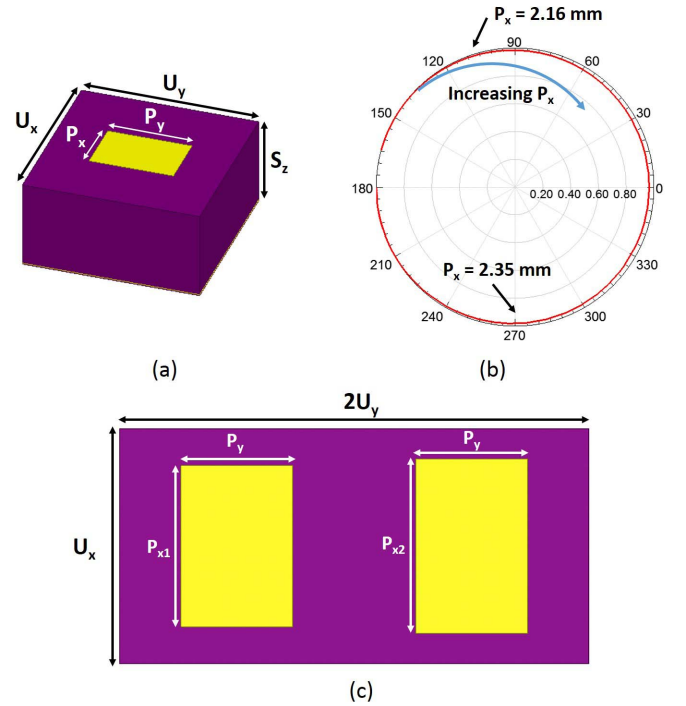


Fig. 5. Single element design for the TE (electric field along x) retroreflection metasurface at 24 GHz. (a) Geometry of the element. Dimensions are $U_x = U_y = 3.149$ mm, $S_z = 1.575$ mm, and $P_y = 0.5$ mm. (b) Polar plot of Γ_{TE} as P_x is swept from 1.5 to 3 mm. (c) Top view of the two-cell TE metasurface. Dimensions are $P_y = 1.5$ mm, $P_{x1} = 2.16$ mm, and $P_{x2} = 2.35$ mm.

Since, we wish to discretize this period into two cells, we choose a unit cell size of

$$U_y = \frac{\Lambda_g}{2} = 3.15 \text{ mm}. \quad (19)$$

A. TE Metasurface

1) *Metasurface Element Design:* For the TE polarization, we implement the required reflection coefficient using a ground-backed dipole array. We have shown in previous works that: 1) this structure contains Huygens' source characteristics when operated in reflection mode [41], [48] and 2) by tuning the length of the dipole, one can vary the phase of Γ_{TE} by a phase range approaching 360° [41], [49], with

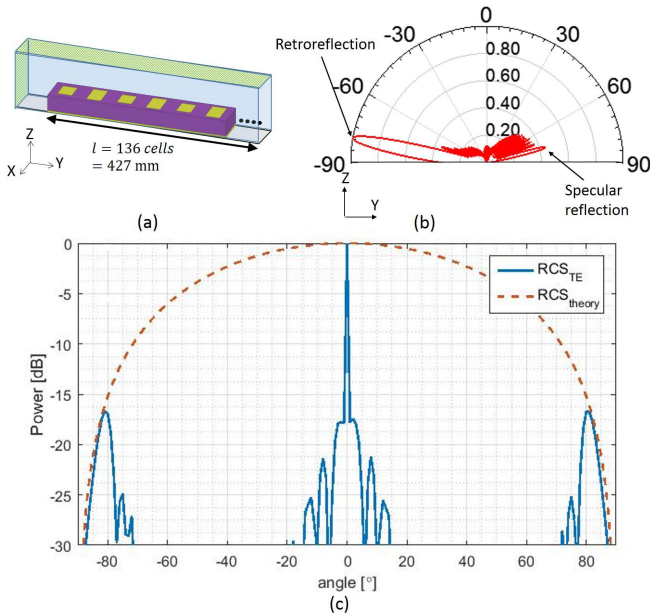


Fig. 6. Simulated results for the TE retroreflection metasurface at 24 GHz. (a) Geometry of the finite element (1-D finite) simulation. The x -directed (blue) faces are periodic boundaries; the y -directed and top z -directed faces are radiation boundaries; the bottom z -directed face is a copper layer. (b) Simulated scattering pattern is plotted for $\phi = 90^\circ$ (the yz plane) (c) Simulated monostatic RCS for the metasurface (blue solid line) is plotted alongside the theoretical RCS of a metallic plate with the same effective aperture, placed normal to the incident radiation (red dotted line) (see Fig. 7 for further explanation).

minimal loss. Fig. 5(a) shows the unit cell geometry of the proposed metasurface element. We design the element on an RT/Duroid 5880 Laminate board from Rogers Corporation, with a thickness of $S_z = 1.575$ mm and $17.8 \mu\text{m}$ ($1/2 \text{ oz}$) copper cladding. The cell size is $U_x = U_y = 3.15$ mm, and the dipole width is $P_y = 0.5$ mm. We investigate the reflection characteristics of this structure by performing full-wave electromagnetic simulation using Ansys HFSS. We terminate the unit cell with periodic boundaries in the x -direction and y -direction, with phase shifts corresponding to an incident wave at $\theta_i = -82.87^\circ$. With a Floquet wave port from the $+z$ boundary, we simulate the wave incidence and observe the reflection coefficient (Γ_{TE}) caused by the unit cell, as we sweep the dipole length from $P_x = 1.5$ to 3 mm. Fig. 5(b) plots Γ_{TE} as a function of the dipole length. As expected, one observes a phase change approaching 360° with relatively low loss. As noted in Fig. 5, operation points $P_{x1} = 2.16$ mm and $P_{x2} = 2.35$ mm differ in phase by about 180° . We choose these to be the operation points for the TE retroreflection metasurface.

2) *Periodic Metasurface Simulation:* Upon choosing the dipole cell lengths P_{x1} and P_{x2} , we place them adjacent to each other and simulate the scattering properties of the resultant binary Huygens' metasurface. Fig. 5(c) shows the top view of one period of this metasurface. Two simulations are performed. First, we perform a 2-D infinitely periodic extension of the metasurface using the Floquet simulation described earlier for the single-element analysis. From this simulation, we find the scattered power into the retro and

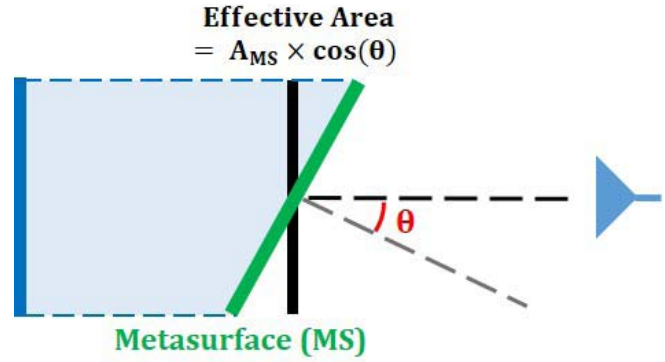


Fig. 7. Effective area of the metasurface (black rectangle) which is determined by the projection of the horn onto the metasurface (this is shown by the blue shaded area). The effective area is calculated by multiplying the area of the metasurface by the angle (θ) that the horn makes with the normal of the metasurface.

specular modes to be 94% and 6%, respectively. This demonstrates very efficient retroreflection and suppression of specular reflection. Second, we truncate the metasurface to 136 cells in the y -direction to simulate the scattering characteristics of a finite metasurface. (We keep the simulation periodic in the x -direction—where the fields are invariant from element to element—to conserve computational resources.) Fig. 6(a) shows a diagram of the truncated (1-D finite) metasurface simulation. As shown in the diagram, we leave an appreciable air gap of $\lambda_0/2$ in the $\pm x$ -direction and $\pm z$ -direction, and simulate radiation boundaries using perfectly matched layers. Upon the illumination of a plane wave at 82.87° , Fig. 6(b) shows the simulated scattering pattern (bistatic RCS) of the resultant structure in the $\phi = 90^\circ$ plane (yz plane). In this scattering pattern, one clearly observes a strong retroreflection component along with a weak specular component. Fig. 6(c) shows the monostatic RCS in the $\phi = 90^\circ$ plane (yz plane). The red dotted line indicates the power that would be reflected by a metallic plate which: 1) occupies the same effective aperture as the metasurface and 2) is placed normal to the incoming wave, as shown in Fig. 7. As the size of this effective aperture scales with $\cos\theta$, the RCS of this plate scales with $\cos^2\theta$ [7]. Since a metal plate illuminated from broadside reflects with 100% aperture efficiency, its monostatic RCS as plotted in Fig. 6(c) provides a measure on the effectiveness of the metasurface, after one properly accounts for the size of the aperture, which varies with the illumination angle. At the angle of $\pm 82^\circ$, the binary Huygens' metasurface achieves an RCS of -0.3 dB compared to the metallic plate, which is equivalent to an aperture efficiency of 93%. Hence, very efficient retroreflection is achieved at near the angle of designed retroreflection.

B. TM Metasurface

1) *Metasurface Element Design:* We design the TM metasurface in a similar fashion to the TE counterpart, but with a different metasurface element. At near-grazing angles, the electric field component of a TM polarized wave points predominantly in the z - (vertical) direction, which couples ineffectively to metallic dipole strip elements on the metasurface. Instead, we seek to couple to the magnetic field using an

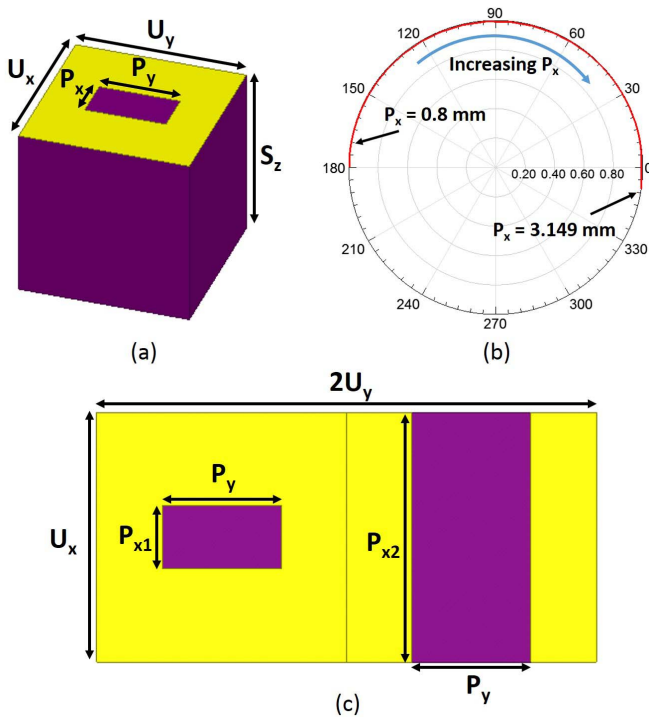


Fig. 8. Single element design for the TM (magnetic field along x) retroreflection metasurface at 24 GHz. (a) Geometry of the element. Dimensions are $U_x = U_y = 3.149$ mm, $S_z = 3.175$ mm, and $P_y = 1.5$ mm. (b) Polar plot of Γ_{TM} as P_x is swept from 0 to 3.149 mm. (c) Top view of the two-cell TM metasurface. Dimensions are $P_y = 1.5$ mm, $P_{x1} = 0.8$ mm, and $P_{x2} = 3.149$ mm.

array of slots—Babinet’s equivalent to the dipole array [50]. Fig. 8(a) shows a schematic of the metasurface element. In this element, a rectangular slot of size $P_x \times P_y$ is etched atop a unit cell with a thickness of $S_z = 3.175$ mm (125 mil), and the same periodicity as the TE counterpart ($U_x = U_y = 3.149$ mm). As with the TE counterpart, we design the metasurface on a Rogers RT/Duroid 5880 laminate board with $17.8 \mu\text{m}$ (1/2 oz) copper cladding on both sides.

We sweep the length of the slot P_x , to tune the coupling dynamic between the ground-backed slot array and the incoming/outgoing waves, which in turn tune the reflection coefficient Γ_{TM} . Fig. 8(b) plots Γ_{TM} as a function of the slot length P_x as we sweep it from 0 to 3.149 mm. Simulations are performed using the Floquet formulation as previously explained for the TE metasurface element. As can be observed, Γ_{TM} attains near-unity magnitude, but its phase variation covers over 190° , which is a notable decrease from the near 360° phase range obtained from the TE counterpart. This in large part is due to the fact that in transforming our metasurface from TE to TM operation, we retained the original substrate dielectric and the ground plane, whereas in a true Babinet’s equivalent, one would replace those with a material of proper magnetic permeability and a magnetic conductor. Despite our practical decision to settle with a compromised Babinet’s equivalent, the reflection response, as displayed in Fig. 8(b) is sufficient for our purpose for a retroreflecting metasurface design. From this plot, we choose our initial operation points

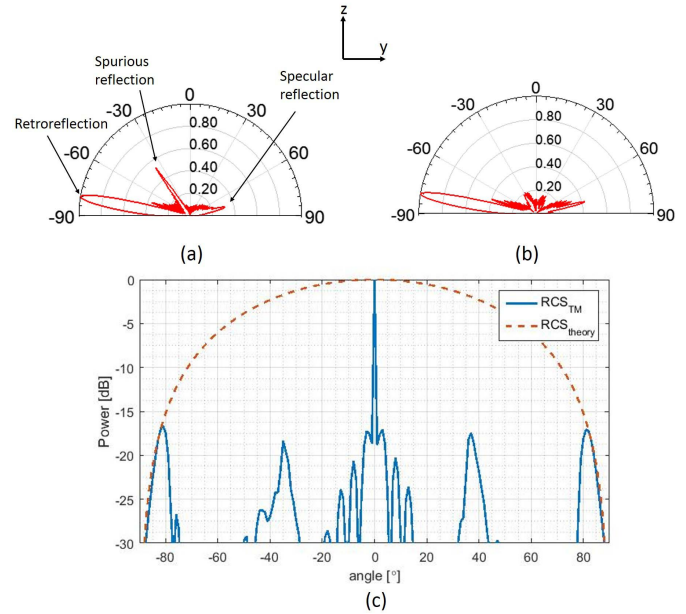


Fig. 9. Simulated results for the TM retroreflection metasurface at 24 GHz. (a) Simulated scattering pattern was plotted (the yz plane). (b) Simulated scattering pattern with absorbers on both ends of the metasurface. (c) Simulated monostatic RCS for the metasurface (blue solid line) plotted alongside the theoretical RCS of a metallic plate with the same effective aperture, placed normal to the incident radiation (red dotted line) (see Fig. 7 for further explanation).

$P_{x1} = 0.8$ mm and $P_{x2} = 3.149$ mm to conduct the two-cell simulation which is as follows.

2) *Periodic Metasurface Simulation*: Once we have chosen the slot dimensions for the two unit cells that occupy a single grating period as shown in Fig. 8(c), we again perform a Floquet simulation that gives us the scattering parameters for a 2-D infinite extension of this binary Huygens’ metasurface. From the simulation, we find that the scattered power into the retro and specular reflection modes to be 84.3% and 15.5%, respectively. We surmise that the existence of this weak specular reflection is caused by differing mutual coupling effects, now that the two elements are placed adjacent to one another. We hence attempt to reoptimize the retroreflector by tuning the length P_{x1} in the Floquet simulation of the binary Huygens’ metasurface. We find that retroreflection is reoptimized when $P_{x1} = 1.6$ mm, at which point, the power efficiencies for retro and specular reflections are 99.1% and 0%, respectively. While the original and reoptimized values of P_{x1} seem to largely differ, they should only affect a slight variation in the reflection coefficient of the metasurface cell, since both slot dimensions are quite far away from resonance. Under this reoptimization, the simulation once again demonstrates very efficient retroreflection and highly suppressed specular reflection.

We then truncate the metasurface to 136 cells in the y -direction to simulate the scattering characteristics of a finite metasurface. The same boundary conditions were applied as in the case of the TE metasurface. Fig. 9(a) shows the simulated scattered pattern of the resultant structure in the $\phi = 90^\circ$ plane (yz plane). This again shows a strong retroreflection component along with a weak specular component. Fig. 9(c)

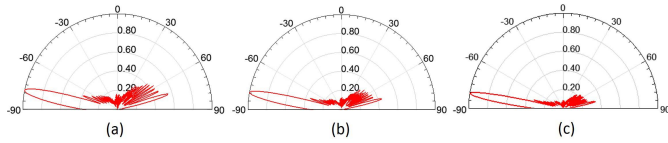


Fig. 10. Comparison between three 1-D finite simulations at 24 GHz. (a) 100 cell—maximum occurs at -79° . (b) 136 cell—maximum occurs at -80° . (c) 200 cell—maximum occurs at -81° .

shows the monostatic RCS in the $\phi = 90^\circ$ plane (yz plane), and this also shows nearly 100% retroreflection at $\pm 82^\circ$ when considering the effective aperture of the board, and depicted by the red dotted line that indicates the maximum power that could be reflected given the size of the board.

3) *Spurious Reflection*: When observing Fig. 9(a), it is evident that the design of the metasurface produces strong retroreflection and suppressed specular reflection. However, the spurious reflection at 37° is a little peculiar in terms of grating theory. Per grating theory, there should only be two modes that are in the propagating regime. We, therefore, hypothesize that this could be caused by coupling of the incident wave to surface waves, which then reradiate to free space. To test this hypothesis, we create, in simulation, a lossy material on both ends of the metasurface. This is done so that if surface waves were to exist within the dielectric, they would get absorbed by the lossy material and, therefore, will not contribute to the generation of spurious reflection. Fig. 9(b) shows the radiation pattern with this adjustment, which indeed proves that the spurious mode originates from the coupling into surface waves and reradiation at the edge of the metasurface. However, the power that is retroreflected is reduced by 0.8 dB, while the specular reflection increases by 2.2 dB using this new design, and thus has its own limitations.

4) *Optimization*: It is important to notice that when doing finite simulations, the retroreflection direction is not exactly that which we designed for. If we look at Fig. 9, we see that the direction of the retroreflected mode is maximal at -80° , whereas the designed angle was -82.87° . The reason for this difference is due to the finite size of the metasurface. A way to counteract this is by designing a metasurface with a slightly larger angle in mind, such that when the structure is reduced to a finite size, it will align with the desired retroreflection angle. Another option is to fabricate a board that is larger, as that will also enable the reflected angle to be closer to the -82.87° , as shown in Fig. 10. As the size of the board increases from 100 cells to 200 cells, the reflected angle changes from -79° to -81° .

C. Bandwidth Analysis

While the binary Huygens' metasurface is designed for perfect retroreflection only at a single frequency, the design methodology of suppressing specular reflection and the usage of relatively large, nonresonant elements are a principle which applies over a wide operational bandwidth. Fig. 11 shows the monostatic RCS for the TM metasurface for a range of frequencies surrounding the design frequency of 24 GHz, compared against the monostatic RCS of a perfect reflector with the same physical aperture. As shown,

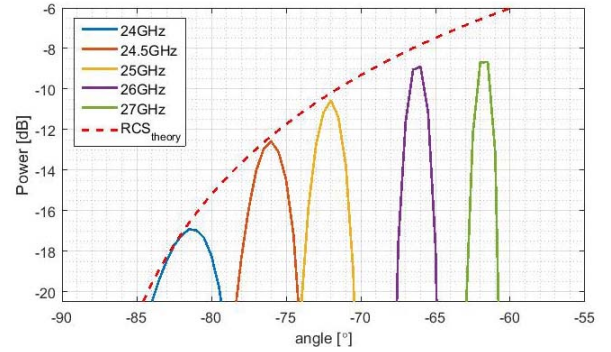


Fig. 11. Monostatic RCS at -82.87° as the frequency is swept from 24 to 27 GHz. The frequencies (from left to right) are: 24, 24.5, 25, 26, and 27 GHz. Red dashed line: reflection strength at perfect aperture efficiency. All plots are normalized such that a reflector with perfect aperture efficiency retroreflects 0 dB upon normal incidence.

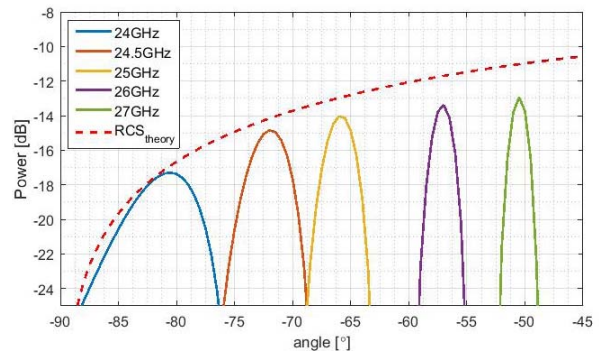


Fig. 12. Bistatic RCS at -82.87° as the frequency is swept from 24 to 27 GHz. The incident angle is kept constant at -82.87° . The frequencies (from left to right) are: 24, 24.5, 25, 26, and 27 GHz. Red dashed line: reflection strength at perfect aperture efficiency. All plots are normalized such that a reflector with perfect aperture efficiency reflects 0 dB toward broadside.

the binary Huygens' metasurface retroreflects with a reasonable efficiency (> -2 dB aperture efficiency) for a frequency range from 24 to 27 GHz. Within this frequency range, the retroreflection angle shifts from -80° to -62° , in accordance to (14). Fig. 12 shows the bistatic RCS for this same range of frequencies, incident on the metasurface from an angle of 82.87° . One can observe that reasonable anomalous reflection (> -2 dB aperture efficiency) is also achieved for this range of frequencies, but the reflection angle deviates from the retro direction due to a beam squinting effect. The reflection angle can be obtained by solving (12) and (13) for the $m = -1$ diffraction order. As we report in [51] and [52], one can achieve perfect anomalous reflection using a binary Huygens' metasurface specifically designed for that purpose.

While we show results only for the TM metasurface, the TE counterpart exhibits a very similar behavior over a comparable bandwidth. Hence, the binary Huygens' metasurfaces boast a wide operational bandwidth of 11.8%, though the retroreflection angle changes within this operation frequency, as dictated by (12) and (13).

IV. MEASUREMENTS

A. TE Metasurface

The TE metasurface is fabricated with 136 cells in the y -direction (the same number of cells that are used for the 1-D

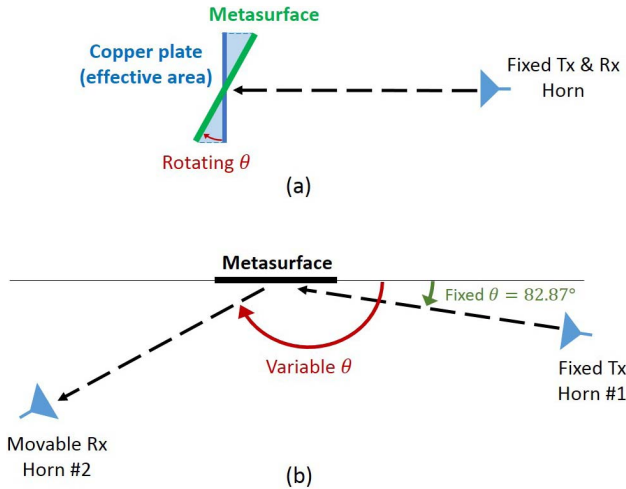


Fig. 13. (a) Monostatic RCS setup with the metasurface (green) which rotates on a stage. The effective area is shown as the area that is normal to the propagating direction of the horn. (b) Bistatic RCS setup: there are limitations on the variable angle in this setup because the movable receiver horn can only measure angles $\pm 4^\circ$ from the fixed horn.

finite simulation), and 87 cells in the x -direction ($428 \text{ mm} \times 275 \text{ mm}$). Two types of measurements are done; monostatic and bistatic RCS. Fig. 13 shows the monostatic and bistatic RCS setup.

1) *Monostatic RCS*: The monostatic RCS measurements are carried out in an anechoic chamber, where we place a vertically polarized, K -band horn on one end of the chamber, and place the metasurface on a rotatable stage 5.3 m away from the horn. This distance corresponds to the far-field of the wave. The S_{11} signal is obtained using the time gating function on the vector network analyzer (VNA) because the reflection due to the horn captured a major component to the S_{11} signal, and thus time gating to measure the received signal around the time of interest allows us to measure the reflection from the metasurface accurately and isolate it from the effects of the reflections due to other sources.

The monostatic RCS measurements are then compared to those of a copper plate with the same effective area. Fig. 14 shows this comparison, where at $\pm 81^\circ$, the retroreflected power is only 0.1 dB smaller than the effective copper plate, which corresponds to 98% aperture efficiency. Therefore, when considering the effective aperture, it is seen that most of the power is coupled into an angle very close to retroreflection.

2) *Bistatic RCS*: The bistatic RCS is measured with an experimental setup depicted in Fig. 13(b). The metasurface was placed on a platform between two arms as shown in Fig. 15. The S_{21} signal received from the Rx horn is measured using a VNA where two steps were taken. First, an S_{21} background level is recorded into memory (without the metasurface on the platform), and second, we place the metasurface on the platform and measure the S_{21} again with the subtraction of the background. The resulting measurements are seen in Fig. 16 where the bistatic RCS of the TE metasurface is measured alongside the bistatic RCS for a copper plate of the same size. It can be inferred that the retroreflection from the metasurface at -82.87° corresponds to 93% of the power that specularly reflects off a copper plate of the same size, while

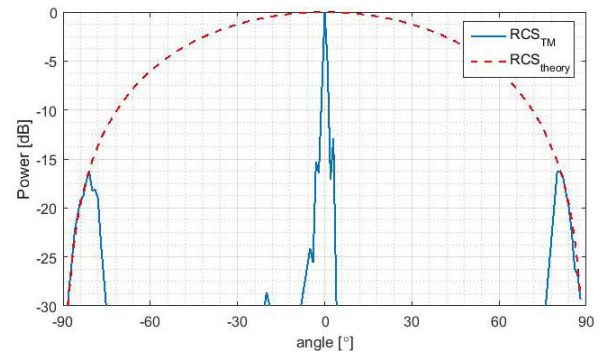


Fig. 14. Monostatic RCS measurement for the TE board (blue solid line) at 24 GHz, and an effective aperture (red dotted line). The angle is with respect to broadside incidence.

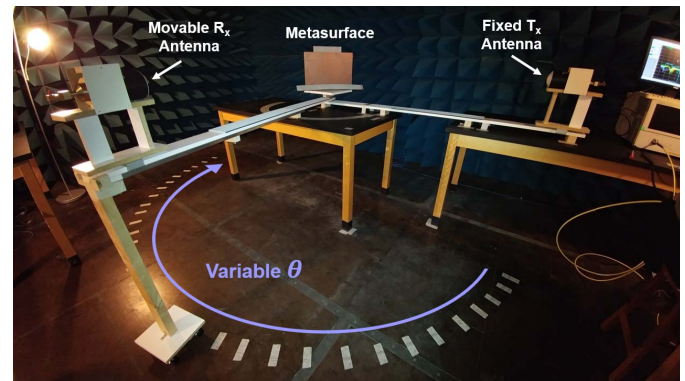


Fig. 15. Bistatic RCS measurement setup.

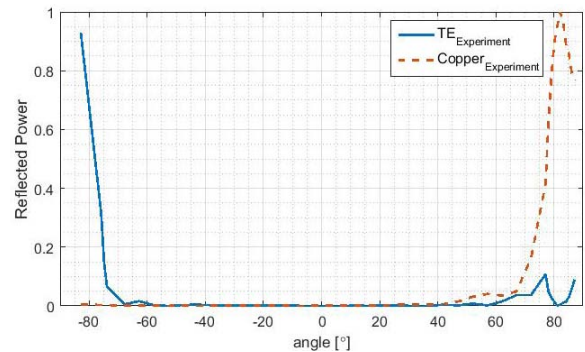


Fig. 16. Bistatic RCS measurement comparing the TE metasurface (blue solid line) with a copper plate (red dotted line) at 24 GHz. This figure is normalized to the specular reflection power of a copper plate.

the specular reflection of the metasurface is greatly reduced to only 10% when compared to a copper plate. We have obtained much stronger suppression at the specular angle as evidenced by the dip at $+82.87^\circ$. However, the finite size of the metasurface and the angular width of the incident beam created appreciable reflection at an angle near the specular angle, for which the suppression is less dramatic. We can obtain greater efficiency and retroreflection at the designed angle of -82.87° by increasing the size of the board.

B. TM Metasurface

The TM metasurface is also fabricated with 136 cells in the y -direction (again the same number of cells that are used for the 1-D finite simulation), and 87 cells in the x -direction

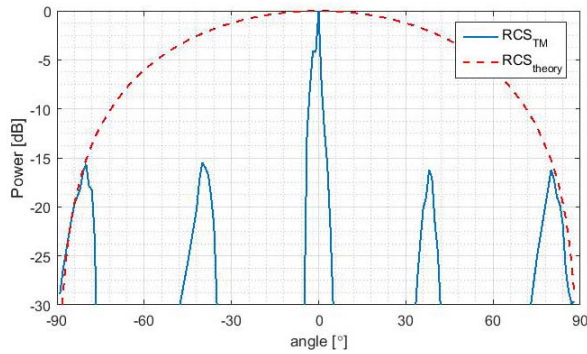


Fig. 17. Monostatic RCS measurement for the TM board (blue solid line) at 24 GHz and the theoretical effective aperture (red dotted line).

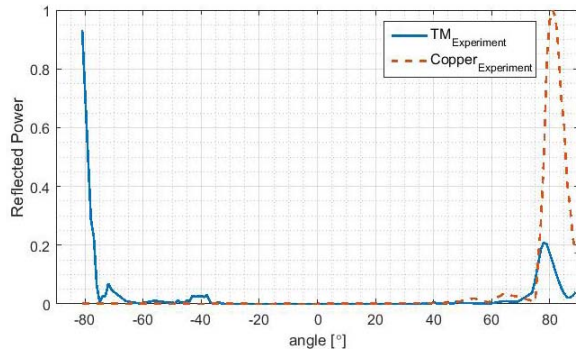


Fig. 18. Bistatic measurement comparison between the TM board (blue solid line) and a copper plate (red dotted line) at 24 GHz. This figure is normalized the specular reflection power of a copper plate.

(428 mm \times 275 mm). We measure the monostatic and bistatic RCS of this metasurface in a similar manner to its TE counterpart.

1) *Monostatic RCS*: Fig. 17 shows the monostatic RCS of the TM board, and when it is compared to an effective copper plate at $\pm 82.87^\circ$, there is a difference of 0.2 dB, which is an aperture efficiency of 95%. This again shows that most of the power is coupled into the retroreflected mode. Fig. 17 is also consistent with what we found in the simulation where the retroreflected power at $\pm 82.87^\circ$ and $\pm 37^\circ$ is in the range of -18 to -15 dB.

2) *Bistatic RCS*: The bistatic experiment is done using an incident angle of -81° rather than -82.87° , because we find this to be the optimal retroreflection angle given the finite size of the metasurface. Fig. 18 shows the bistatic RCS of the TM board where there is a strong retroreflected component and a suppressed specular component. The retroreflection from the metasurface at -81° is approximately 93% of the power that specularly reflects off a copper plate, while the remaining power reflected from the metasurface is very minimal. Once more this shows that there is a strong coupling of the incident wave at -81° to the retroreflected mode, whereas the specular mode is greatly suppressed.

V. CONCLUSION

We have reported binary Huygens' metasurfaces that achieve strong retroreflection at near-grazing incidence for

both TE and TM polarizations. These binary Huygens' metasurfaces feature aggressive discretizations of only two elements per grating period, implemented by ground-backed dipole (for the TE surface) and slot (for the TM surface) arrays. We have reported their design procedure, and through simulations and experiments, we have demonstrated their capability to achieve strong retroreflection and greatly suppress specular reflection. Experimental demonstration shows the achievement of retroreflection at 90%–95% aperture efficiency for both polarizations. In departure from contemporary metasurfaces, the binary Huygens' metasurfaces introduced here boast the single-layer construction, large unit cell sizes, and simple elements, which lead to advantages in relaxed precision tolerance, simple fabrication, and robust operation. These advantages make the binary Huygens' metasurface an attractive candidate for the design of next generation cost-efficient, low profile, and effective retroreflectors for millimeter-wave and terahertz frequencies.

REFERENCES

- [1] P. Villoresi *et al.*, "Experimental verification of the feasibility of a quantum channel between space and earth," *New J. Phys.*, vol. 10, p. 033038, Mar. 2008.
- [2] G. C. Gilbreath *et al.*, "Large-aperture multiple quantum well modulating retroreflector for free-space optical data transfer on unmanned aerial vehicles," *Opt. Eng.*, vol. 40, no. 7, p. 1348–1357, 2001.
- [3] L. Zhou, J. M. Kahn, and K. S. J. Pister, "Corner-cube retroreflectors based on structure-assisted assembly for free-space optical communication," *J. Microelectromech. Syst.*, vol. 12, no. 3, pp. 233–242, Jun. 2003.
- [4] D. D. Nelson, M. S. Zahniser, J. B. McManus, C. E. Kolb, and J. L. Jiménez, "A tunable diode laser system for the remote sensing of on-road vehicle emissions," *Appl. Phys. B, Lasers Opt.*, vol. 67, no. 4, pp. 433–441, 1998.
- [5] I. Kwan and J. Mapstone, "Interventions for increasing pedestrian and cyclist visibility for the prevention of death and injuries," *Cochrane Library*, vol. 4, p. CD003438, Oct. 2006.
- [6] Y. Shang, S. Xiao, and Z. Shen, "Edge-on backscattering enhancement based on quasi-superdirective reradiation," *IEEE Antennas Wireless Propag. Lett.*, vol. 14, pp. 539–542, 2015.
- [7] B. R. Mahafza, *Radar Systems Analysis and Design Using MATLAB*. London, U.K.: Chapman & Hall, 2005.
- [8] J. L. Zurasky, "Cube corner retroreflector test and analysis," *Appl. Opt.*, vol. 15, no. 2, pp. 445–452, 1976.
- [9] D. Bird, "Design and manufacture of a low-profile radar retro-reflector," Thales Commun., Clarksburg, MD, USA, Tech. Rep., Dec. 2005.
- [10] M. L. Biermann, W. S. Rabinovich, R. Mahon, and G. C. Gilbreath, "Design and analysis of a diffraction-limited cat's-eye retroreflector," *Opt. Eng.*, vol. 41, no. 7, pp. 1655–1661, 2002.
- [11] D. C. O'Brien, G. E. Faulkner, and D. J. Edwards, "Optical properties of a retroreflecting sheet," *Appl. Opt.*, vol. 38, no. 19, pp. 4137–4144, 1999.
- [12] Y. Kuga and A. Ishimaru, "Retroreflectance from a dense distribution of spherical particles," *J. Opt. Soc. Amer. A, Opt. Image Sci.*, vol. 1, no. 8, pp. 831–835, 1984.
- [13] B. W. Hapke, R. M. Nelson, and W. D. Smythe, "The opposition effect of the moon: The contribution of coherent backscatter," *Science*, vol. 260, no. 5107, pp. 509–511, 1993.
- [14] A. R. McGurn, "Enhanced retroreflectance effects in the reflection of light from randomly rough surfaces," *Surf. Sci. Rep.*, vol. 10, no. 8, pp. 357–410, 1990.
- [15] R. Beer and D. Marjaniemi, "Wavefronts and construction tolerances for a cat's-eye retroreflector," *Appl. Opt.*, vol. 5, no. 7, pp. 1191–1197, 1966.
- [16] J. J. Snyder, "Paraxial ray analysis of a cat's-eye retroreflector," *Appl. Opt.*, vol. 14, no. 8, pp. 1825–1828, 1975.
- [17] A. Lundvall, F. Nikolajeff, and T. Lindström, "High performing micro-machined retroreflector," *Opt. Exp.*, vol. 11, no. 20, pp. 2459–2473, 2003.

- [18] R. K. Luneburg and M. Herzberger, *Mathematical Theory of Optics*. Oakland, CA, USA: Berkeley Univ. California Press, 1964.
- [19] Y. G. Ma, C. K. Ong, T. Tyc, and U. Leonhardt, "An omnidirectional retroreflector based on the transmutation of dielectric singularities," *Nature Mater.*, vol. 8, pp. 639–642, Jun. 2009.
- [20] W. H. Wee and J. B. Pendry, "Shrinking optical devices," *New J. Phys.*, vol. 11, p. 073033, Jul. 2009.
- [21] Z. Ruan and S. Fan, "Superscattering of light from subwavelength nanostructures," *Phys. Rev. Lett.*, vol. 105, no. 1, p. 013901, 2010.
- [22] R. C. Hansen, "Fundamental limitations in antennas," *Proc. IEEE*, vol. 69, no. 2, pp. 170–182, Feb. 1981.
- [23] N. Yu *et al.*, "Light propagation with phase discontinuities: Generalized laws of reflection and refraction," *Science*, vol. 334, no. 6054, pp. 333–337, Oct. 2011.
- [24] L. C. Van Atta, "Electromagnetic reflector," U.S. Patent 2908002 A, Oct. 6, 1959.
- [25] E. D. Sharp and M. Diab, "Van Atta reflector array," *IRE Trans. Antennas Propag.*, vol. 8, no. 4, pp. 436–438, Jul. 1960.
- [26] R. C. Hansen, "Communications satellites using arrays," *Proc. IRE*, vol. 49, no. 6, pp. 1066–1074, Jun. 1961.
- [27] T. Itoh and R. Mittra, "An analytical study of the echelette grating with application to open resonators," *IEEE Trans. Microw. Theory Techn.*, vol. MTT-17, no. 6, pp. 319–327, Jun. 1969.
- [28] A. Hessel, J. Schmoys, and D. Y. Tseng, "Bragg-angle blazing of diffraction gratings," *J. Opt. Soc. Amer. A, Opt. Image Sci.*, vol. 65, no. 4, pp. 380–384, 1975.
- [29] E. V. Jull, J. W. Heath, Jr., and G. R. Ebbeson, "Gratings that diffract all incident energy," *J. Opt. Soc. Amer.*, vol. 65, no. 4, pp. 557–559, 1977.
- [30] K. A. Jose and K. G. Nair, "Reflector-backed perfectly blazed strip gratings simulate corrugated reflector effects," *Electron. Lett.*, vol. 23, no. 2, pp. 86–87, Jan. 1987.
- [31] H. A. Kalhor, "Electromagnetic scattering by a dielectric slab loaded with a periodic array of strips over a ground plane," *IEEE Trans. Antennas Propag.*, vol. AP-36, no. 1, pp. 147–151, Jan. 1988.
- [32] W. Chen, N. C. Beaulieu, D. G. Michelson, and E. V. Jull, "Off-Bragg blazed rectangular groove gratings for high diffraction efficiency devices," *IEEE Trans. Antennas Propag.*, vol. 61, no. 4, pp. 2342–2347, Apr. 2013.
- [33] K. C. Young, J. W. Ra, U. H. Cho, and J. I. Lee, "Off-Bragg TE blazing of a periodic strip grating on a grounded dielectric," *Electron. Lett.*, vol. 33, no. 17, pp. 1446–1447, Aug. 1997.
- [34] M. Memarian, X. Li, Y. Morimoto, and T. Itoh, "Wide-band/angle blazed surfaces using multiple coupled blazing resonances," *Sci. Rep.*, vol. 7, Feb. 2017, Art. no. 42286.
- [35] C. L. Holloway, M. A. Mohamed, E. F. Kuester, and A. Dienstfrey, "Reflection and transmission properties of a metafilm: With an application to a controllable surface composed of resonant particles," *IEEE Trans. Electromagn. Compat.*, vol. 47, no. 4, pp. 853–865, Nov. 2005.
- [36] R. Leberer and W. Menzel, "A dual planar reflectarray with synthesized phase and amplitude distribution," *IEEE Trans. Antennas Propag.*, vol. 53, no. 11, pp. 3534–3539, Nov. 2005.
- [37] C. L. Holloway, E. F. Kuester, J. A. Gordon, J. O'Hara, J. Booth, and D. R. Smith, "An overview of the theory and applications of metasurfaces: The two-dimensional equivalents of metamaterials," *IEEE Antennas Propag. Mag.*, vol. 54, no. 2, pp. 10–35, Apr. 2012.
- [38] A. Epstein and G. V. Eleftheriades, "Huygens' metasurfaces via the equivalence principle: Design and applications," *J. Opt. Soc. Amer. B, Opt. Phys.*, vol. 33, no. 2, pp. A31–A50, 2016.
- [39] V. S. Asadchy, M. Albooyeh, S. N. Tsvetkova, A. Díaz-Rubio, Y. Ra'di, and S. A. Tretyakov, "Perfect control of reflection and refraction using spatially dispersive metasurfaces," *Phys. Rev. B, Condens. Matter*, vol. 94, no. 7, p. 075142, 2016.
- [40] N. M. Estakhri and A. Alù, "Wave-front transformation with gradient metasurfaces," *Phys. Rev. X*, vol. 6, no. 4, p. 041008, 2016.
- [41] M. Kim, A. M. H. Wong, and G. V. Eleftheriades, "Optical Huygens' metasurfaces with independent control of the magnitude and phase of the local reflection coefficients," *Phys. Rev. X*, vol. 4, no. 4, p. 041042, Dec. 2014.
- [42] J. P. S. Wong, M. Selvanayagam, and G. V. Eleftheriades, "Design of unit cells and demonstration of methods for synthesizing Huygens metasurfaces," *Photon. Nanostruct. Fundam. Appl.*, vol. 12, no. 4, pp. 360–375, Aug. 2014.
- [43] M. Selvanayagam and G. V. Eleftheriades, "Polarization control using tensor Huygens surfaces," *IEEE Trans. Antennas Propag.*, vol. 62, no. 12, pp. 6155–6168, Sep. 2014.
- [44] M. Selvanayagam and G. V. Eleftheriades, "Design and measurement of tensor impedance transmitarrays for chiral polarization control," *IEEE Trans. Antennas Propag.*, vol. 64, no. 2, pp. 414–428, Feb. 2016.
- [45] M. Selvanayagam and G. V. Eleftheriades, "Discontinuous electromagnetic fields using orthogonal electric and magnetic currents for wavefront manipulation," *Opt. Exp.*, vol. 21, no. 12, pp. 14409–14429, 2013.
- [46] M. Selvanayagam and G. V. Eleftheriades, "Circuit modeling of Huygens surfaces," *IEEE Antennas Wireless Propag. Lett.*, vol. 12, pp. 1642–1645, 2013.
- [47] M. Memarian and G. V. Eleftheriades, "Dirac leaky-wave antennas for continuous beam scanning from photonic crystals," *Nature Commun.*, vol. 6, Jan. 2015, Art. no. 5855.
- [48] A. M. H. Wong and G. V. Eleftheriades, "Active Huygens' metasurfaces for RF waveform synthesis in a cavity," in *Proc. 18th IEEE Medit. Electrotech. Conf. (MELECON)*, Apr. 2016, pp. 1–5.
- [49] A. M. H. Wong, P. Christian, and G. V. Eleftheriades, "Binary Huygens' metasurface: A simple and efficient retroreflector at near-grazing angles," in *Proc. United States Nat. Committee URSI Nat. Radio Sci. Meeting (USNC-URSI NRSM)*, Jan. 2017, pp. 1–2.
- [50] C. A. Balanis, *Antenna Theory and Design*, 3rd ed. Hoboken, NJ, USA: Wiley, 2005.
- [51] A. M. H. Wong and G. V. Eleftheriades, "Perfect anomalous reflection with an aggressively discretized Huygens' metasurface," in *Proc. 32nd URSI General Assembly Sci. Symp. Int. Union Radio Sci.*, Aug. 2017, pp. 1–3.
- [52] A. M. H. Wong and G. V. Eleftheriades, "Perfect anomalous reflection with a bipartite Huygens' metasurface," *Phys. Rev. X*, vol. 8, no. 1, p. 011036, 2018.



Alex M. H. Wong (S'00–M'15) received the Ph.D. degree in electrical engineering from the University of Toronto, Toronto, ON, Canada, in 2014.

He then served briefly as a Postdoctoral Fellow at the University of Toronto. He is an Assistant Professor of applied electromagnetics with the Department of Electronic Engineering, City University of Hong Kong (CityU), Hong Kong. He is also a member of the State Key Laboratory of Millimeter Waves, partner Laboratory at CityU.

He has advanced multiple projects in applied electromagnetics on next-generation RF, infrared and optical metasurfaces, superoscillation-based imaging, and radar systems. His current research interests include metasurfaces, metamaterials, and super-resolution systems.

Dr. Wong is a member of the IEEE Antennas and Propagation Society and Microwave Theory and Techniques Society. He has received several accolades which include an IEEE RWP King Award (for the best annual publication by a young author in the IEEE TRANSACTIONS ON ANTENNAS AND PROPAGATION), an URSI Young Scientist Award, a Raj Mittra Grant, IEEE doctoral research awards from the AP and MTT societies, and the National NSERC Canada Graduate Scholarship.



Philip Christian received the B.Sc. degree in mathematics and physics from York University, Toronto, ON, Canada, in 2014, and the M.Eng. and M.A.Sc. degrees in electrical engineering from the University of Toronto, Toronto, ON, Canada, in 2015 and 2017, respectively.

He is currently a Systems Engineer with Thales Canada, Ville de Québec, QC, Canada, where he is involved in integrating sensors for an autonomous train platform. His current research interests include the field of electromagnetics, where

he focused on photonic devices and the design and simulation of reflective metasurfaces.



George V. Eleftheriades (S'86–M'88–SM'02–F'06) received the M.S.E.E. and Ph.D. degrees in electrical engineering from the University of Michigan, Ann Arbor, MI, USA, in 1989 and 1993, respectively.

From 1994 to 1997, he was with the Swiss Federal Institute of Technology, Lausanne, Switzerland. He is currently a Professor with the Department of Electrical and Computer Engineering, University of Toronto, ON, Canada, where he holds the Canada Research/Velma M. Rogers Graham Chair in

Nano- and Micro-Structured Electromagnetic Materials. He is a recognized international authority and pioneer in the area of metamaterials. These are man-made materials which have electromagnetic properties not found in nature. He introduced a method for synthesizing metamaterials using loaded transmission lines. Together with his graduate students, he provided the first experimental evidence of imaging beyond the diffraction limit and pioneered several novel antennas and microwave components using these transmission-line based metamaterials. His research has impacted the field by demonstrating the unique electromagnetic properties of metamaterials; used in lenses, antennas, and other microwave and optical components to drive innovation in fields, such as wireless and satellite communications, defence, medical imaging, microscopy, and automotive radar. He is currently leading a group of graduate students and researchers in the areas of electromagnetic

and optical metamaterials, and metasurfaces, antennas and components for broadband wireless communications, novel antenna beam-steering techniques, far-field super-resolution imaging, radars, plasmonic and nanoscale optical components, and fundamental electromagnetic theory.

Dr. Eleftheriades served as a member of the IEEE Antennas and Propagation (AP)-Society administrative committee from 2007 to 2012. In 2009, he was elected as a fellow of the Royal Society of Canada. He was an IEEE AP-S Distinguished Lecturer from 2004 to 2009. His co-authored papers received numerous awards such as the 2009 Best Paper Award from the IEEE MICROWAVE AND WIRELESS PROPAGATION LETTERS, the R. W. P. King Best Paper Award from the IEEE TRANSACTIONS ON ANTENNAS AND PROPAGATION in 2008 and 2012, and the 2014 Piergiorgio Uslenghi Best Paper Award from the IEEE ANTENNAS AND WIRELESS PROPAGATION LETTERS. He received the Ontario Premier's Research Excellence Award in 2001, the University of Toronto's Gordon Slemon Award in 2001, and the E.W.R. Steacie Fellowship from the Natural Sciences and Engineering Research Council of Canada in 2004. He was a recipient of the 2008 IEEE Kiyu Tomiyasu Technical Field Award and the 2015 IEEE John Kraus Antenna Award, and the Research Leader Award from the Faculty of Applied Science and Engineering of the University of Toronto in 2018. He served as the General Chair of the 2010 IEEE International Symposium on Antennas and Propagation held in Toronto, ON, Canada. He served as an Associate Editor for the IEEE TRANSACTIONS ON ANTENNAS AND PROPAGATION.